Proportion of Grid-forming Wind Turbines in Hybrid GFM-GFL Offshore Wind Farms Integrated with Diode Rectifier Unit Based HVDC System

Yanqiu Jin, Zheren Zhang, and Zheng Xu

***Abstract*—This study analyzes the stability and reactive characteristics of the hybrid offshore wind farm that includes grid-forming (GFM) and grid-following (GFL) wind turbines (WTs) integrated with a diode rectifier unit (DRU) based high-voltage direct current (HVDC) system. The determination method for the proportion of GFM WTs is proposed while considering system stability and optimal offshore reactive power constraints. First, the small-signal stability is studied based on the developed linear model, and crucial factors that affect the stability are captured by eigenvalue analysis. The reactive power-frequency compensation control of GFM WTs is then proposed to improve the reactive power and frequency dynamics. Second, the relationship between offshore reactive power imbalance and the effectiveness of GFM capability is analyzed. Offshore reactive power optimization methods are next proposed to diminish offshore reactive load. These methods include the optimal design for the reactive capacity of the AC filter and the reactive power compensation control of GFL WTs. Third, in terms of stability and optimal offshore reactive power constraints, the principle and calculation method for determining the proportion of GFM WTs are proposed, and the critical proportion of GFM WTs is determined over the full active power range. Finally, case studies using a detailed model are conducted by time-domain simulations in PSCAD/EMTDC. The simulations verify the theoretical analysis results and the effectiveness of the proposed determination method for the proportion of GFM WTs and reactive power optimization methods.**

***Index Terms*—Offshore wind farm, diode rectifier unit, high-voltage direct current (HVDC), grid-forming (GFM) wind turbine, grid-following (GFL) wind turbine.**

I. Introduction

DUE to its superior wind resources, distant offshore wind power is of strategic significance for renewable energy exploitation [1]. The reliable and efficient integration is critical in supporting the development of long-distance and large-capacity offshore wind farms. Currently, offshore wind projects over 80 km are primarily transmitted by modular multilevel converter (MMC) based high voltage direct current (HVDC) systems [2], where the offshore AC voltage is controlled by the offshore MMC, enabling grid-following (GFL) wind turbines (WTs) to operate normally based on a phase-locked loop (PLL) [3]. However, an MMC-based HVDC scheme requires a large and costly offshore MMC platform [4], which restricts the long-distance offshore wind power development.

Applying low-cost and light-weight converters is an effective means of reducing the costs and construction difficulties of offshore platforms [5], [6]. Compared with other topologies, the diode rectifier unit (DRU) has higher reliability, lower cost, and smaller loss [7]. The replacement of the MMC rectifier with a DRU significantly reduces the volume and cost of the offshore platform by 80% and 30%, respectively [8], leading to great potential for offshore wind integration.

However, the commutation voltage of a DRU must be provided by an external AC voltage source. The DRU cannot actively control the offshore AC voltage or support the operation of GFL WTs. Existing solutions for supporting the offshore AC voltage fall into two main categories.

1) An intuitive technical approach is to install additional voltage source equipment to provide centralized offshore AC voltage support, including a voltage source converter (VSC) installed in series [9]-[12] or in parallel [13]-[16] with the DRU and an MMC-HVDC link [17]-[19] or high voltage alternating current (HVAC) link [20], [21] in parallel with the DRU-based HVDC (DRU-HVDC) link. In this manner, the conventional GFL WTs can operate. However, the additional device reduces the economic advantage of the offshore DRU platform [22].

2) To maintain the light-weight offshore DRU platform, WTs can be converted into the grid-forming (GFM) mode to achieve decentralized offshore AC voltage control [23], [24]. According to WT synchronization methods, the existing control strategies for GFM WTs integrated with the DRU mainly include three types: PLL-based [25]-[29], global unified reference frame based [30]-[32], and reactive power frequency droop-based [33]-[37] strategies. Of these, the reactive power-frequency droop-based strategy can realize self-syn-

Manuscript received: April 24, 2024; revised: May 25, 2024; accepted: June 8, 2024. Date of CrossCheck: June 8, 2024. Date of online publication: July 15, 2024.

This work was supported by the Research Project of China Southern Power Grid Co., Ltd. (No. 030400KK52220008 (GDKJXM20220327)).

Y. Jin, Z. Zhang (corresponding author), and Z. Xu are with the Department of Electrical Engineering, Zhejiang University, Hangzhou 310027, China (e-mail: 12210008@zju.edu.cn; 3071001296zhang@zju.edu.cn; xuzheng007@zju.edu.cn).

DOI: 10.35833/MPCE.2024.000432

chronization and equal distribution of reactive power among WTs without relying on high-speed communication or PLL. This means it has higher reliability and application potential [38].

To date, all commissioned offshore WTs have operated in the GFL mode, while the GFM WT suitable for DRU-based transmission has remained in the research stage and has not been applied in practical projects. Compared with the GFL WT, the technical maturity and operational experience of the GFM WT are much lower. Thus, adopting the GFM mode for all WTs at this stage results in higher investment and maintenance costs for the offshore wind farm. In addition, the hybrid scheme of GFM and GFL WTs is also a potential means of upgrading existing GFL wind farms that wish to be integrated with economical DRUs. Therefore, studying the DRU-based integration scheme for the hybrid offshore wind farm with both GFM and GFL WTs is valuable and practical.

However, in most of the existing literature, only those cases in which all WTs are in the GFM mode have been considered [25]-[37]. Reference [39] examines a hybrid offshore wind farm, in which GFM and GFL WTs are connected to multiple DRU stations with higher investments. A lack of GFM WTs may not support the AC voltage for the DRU and GFL WTs, and insufficient GFM WTs as reactive power balancing nodes can experience current saturation and lose GFM capabilities. Therefore, determining the appropriate proportion of GFM WTs is essential for the stable operation of the hybrid GFM-GFL offshore wind farm integrated with the DRU-HVDC system, which requires further research.

To fill in the research gap, the determination method for the proportion of GFM WTs in the hybrid GFM-GFL offshore wind farm integrated with the DRU-HVDC system, considering the system stability and optimal offshore reactive power constraints, is proposed in this paper. The main contributions of this study are as follows.

1) The potential effects of the proportion of GFM WTs, the offshore reactive load, and the proportional coefficient of the reactive power-frequency controller on the system stability are revealed. The offshore reactive power optimization methods are proposed, including the optimal design for the reactive capacity of AC filter and the reactive power compensation control of GFL WTs.

2) The determination method for the proportion of GFM WTs is proposed while considering system stability and optimal offshore reactive power constraints. The definition and the calculation method for the critical proportion are proposed. Accordingly, the critical proportion of GFM WTs over the full active power range is determined.

The remainder of this paper is organized as follows. In Section II, the model of hybrid GFM-GFL offshore wind farm integrated with DRU-HVDC system is described. The system stability is analyzed in Section III. Section IV describes the proposed offshore reactive power optimization methods. The method for determining the proportion of the GFM WTs is presented in Section V. Section VI describes the simulation verification via case studies. Section VII summarizes the findings.

II. Model of Hybrid GFM-GFL Offshore Wind Farm Integrated with DRU-HVDC System

Figure 1 shows the structure of hybrid GFM-GFL offshore wind farm integrated with the DRU-HVDC system. A large-capacity offshore wind farm includes numerous GFM and GFL WT clusters. GFM WTs support offshore AC voltage for the normal operation of the DRU and GFL WTs. The offshore wind power is collected to the point of common coupling (PCC) through AC cables and transmitted to the onshore grid via a DRU rectifier, HVDC cables, and an MMC inverter. The system model is established as differential-algebraic equations for stability analysis.

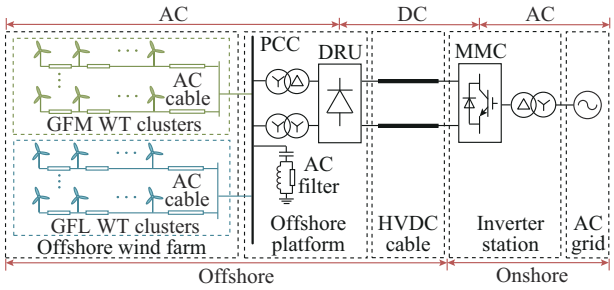

Fig. 1. Structure of hybrid GFM-GFL offshore wind farm integrated with DRU-HVDC system.

A. GFM WT

The DC voltage of the back-to-back converters of the GFM WT is kept constant by the machine-side converter, which can be equivalent to a constant DC voltage source. The GFM capability is realized by the grid-side converter (GSC) that uses active power-voltage and reactive power-frequency controllers as well as voltage and current proportional-integral (PI) controllers. The AC side of GSC is connected to the LC filter and WT transformer, as shown in Fig. 2.

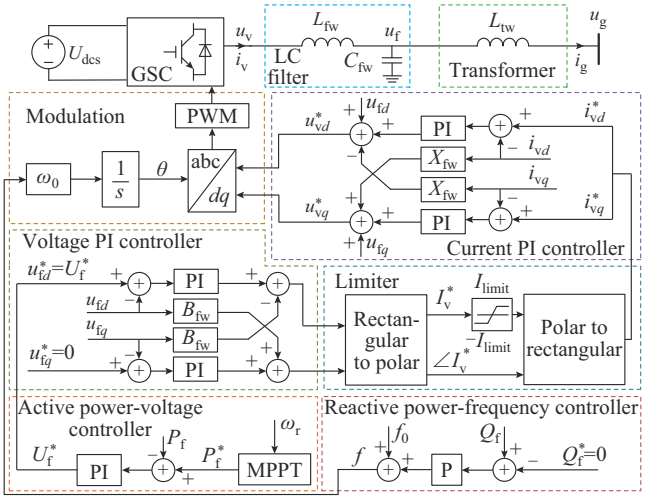

Fig. 2. Model of GFM WT.

In Fig. 2, L_{fw}, X_{fw}, C_{fw}, and B_{fw} are the inductance, reactance, capacitance, and susceptance of LC filter, respectively; L_{tw} is the transformer leakage inductance; U_{dcs} is the equivalent DC voltage; u_v and i_v are the voltage and current on the AC side of GSC, respectively; u_f and u_g are the volt-

ages on the valve and grid sides of transformer, respectively; i_g is the currnet on the grid side; U_f, P_f, and Q_f are the voltage amplitude, active power, and reactive power on the valve side of transformer, respectively; f_0 and ω_0 are the rated frequency and angular frequency, respectively; f, ω, and θ are the actual frequency, angular frequency, and phase of WT, respectively; I_{limit} is the reference current limit; the superscript * denotes the reference value; subscripts d and q denote the d- and q-axis components, respectively; and PWM is short for pulse width modulation.

Due to the operational characteristics of the DRU, the control variables of the GFM WTs integrated with the DRU are matched as the active power-voltage amplitude and reactive power-frequency [36]. As the absorbed reactive power of DRU is determined by its transmitted active power, the active power of the GFM WTs is an independent variable, whereas the reactive power of the GFM WTs is not. For the active power-voltage controller, the active power can track its reference accurately. Therefore, the PI control is adopted due to its good performance in tracking DC references. The reference active power is generated using the maximum power point tracking (MPPT). GFM WTs serve as reactive power balancing nodes in the hybrid GFM-GFL offshore wind farm integrated with the DRU-HVDC system. Thus, the reactive power-frequency controller is designed as a proportional controller to enable the reactive power of WT to fluctuate and maintain offshore reactive power balance under different operating conditions [36]. The active power-voltage and reactive power-frequency controllers are defined as:

$$U_f^* = \left(K_p + \frac{1}{T_p s}\right)(P_f^* - P_f) \tag{1}$$

$$f = K_{qm}(Q_f - Q_f^*) + f_0 \tag{2}$$

where K_p and T_p are the proportional and integral coefficients of the active power-voltage controller, respectively; and K_{qm} is the proportional coefficient of the reactive power-frequency controller.

The reference voltage amplitude U_f^* from the active power-voltage controller is fed to the voltage PI controller, which regulates the d- and q-axis voltages to U_f^* and 0, respectively, and generates the reference current as:

$$i_{vd}^* = \left(K_v + \frac{1}{T_v s}\right)(u_{fd}^* - u_{fd}) - B_{fw} u_{fq} \tag{3}$$

$$i_{vq}^* = \left(K_v + \frac{1}{T_v s}\right)(u_{fq}^* - u_{fq}) + B_{fw} u_{fd} \tag{4}$$

where K_v and T_v are the proportional and integral coefficients of the voltage PI controller, respectively.

The current PI controller regulates the output voltage to maintain the output current as the reference. Considering the modulation ratio as m_m, we can calculate the voltage at the AC side of GSC as:

$$u_{vd} = m_m\left[\left(K_{cm} + \frac{1}{T_{cm} s}\right)(i_{vd}^* - i_{vd}) - X_{fw} i_{vq} + u_{fd}\right] \tag{5}$$

$$u_{vq} = m_m\left[\left(K_{cm} + \frac{1}{T_{cm} s}\right)(i_{vq}^* - i_{vq}) + X_{fw} i_{vd} + u_{fq}\right] \tag{6}$$

where K_{cm} and T_{cm} are the proportional and integral coefficients of the current PI controller, respectively.

B. DRU Station

Figure 3 shows the model of the DRU-HVDC system, where u_r is the PCC voltage; i_r is the DRU current; P_r and Q_r are the active and reactive power of the DRU, respectively; X_{tr} and T are the leakage reactance and transformer ratio of the transformer, respectively; Q_{filter} is the reactive power of the AC filter; L_{fr} is the smoothing inductance; R_{dc}, L_{dc}, and C_{dc} are the resistance, inductance, and capacitance of the HVDC cable, respectively; I_{dcr} and I_{dci} are the DC currents on the rectifier and inverter sides, respectively; and U_{dcr} and U_{dci} are the DC voltages on the rectifier and inverter sides, respectively.

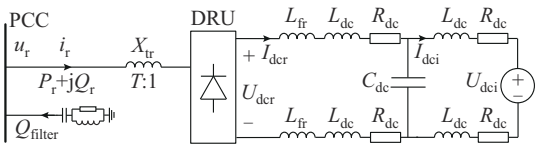

Fig. 3. Model of DRU-HVDC system.

Similar to the line-commutated converter with a trigger angle of 0°, the DC voltage of the 12-pulse DRU satisfies:

$$U_{dcr} = \frac{6\sqrt{2}}{\pi T} U_r - \frac{6X_{tr}}{\pi} I_{dcr} \tag{7}$$

where U_r is the root mean square value of PCC voltage.

The active power and reactive power of the DRU satisfy:

$$P_r = 1.5(i_{rd} u_{rd} + i_{rq} u_{rq}) \tag{8}$$

$$Q_r = 1.5(i_{rd} u_{rq} - i_{rq} u_{rd}) \tag{9}$$

The ratio of Q_r to P_r is expressed as:

$$\tan\varphi = \frac{Q_r}{P_r} = \frac{2\mu - \sin 2\mu}{1 - \cos 2\mu} \tag{10}$$

where the overlap angle μ is:

$$\mu = \arccos\left(1 - \frac{2X_{tr} T I_{dcr}}{\sqrt{2}\, U_r}\right) \tag{11}$$

The DC power of the DRU is expressed as:

$$P_{dcr} = U_{dcr} I_{dcr} \tag{12}$$

P_{dcr} is approximately equal to P_r. Then, the model of DRU station can be obtained using (7)-(12). Except for the DRU station and GFM WTs, the other components, including the GFL WTs, are conventional devices [40]. Their detailed models are not presented here for space purposes.

C. System Small-signal Model

Each WT is modeled under its local reference frame generated by the reactive power-frequency controller or PLL. It is necessary to define a common reference frame to construct the entire system model. The reference frame of a single GFM WT converter is set as the common reference frame. The models of the AC cables and DRU station are established in the common reference frame. The variables at the common points of other WTs and AC cables are transformed between the local and common reference frames.

When (1) - (12) are linearized and intermediate variables are eliminated, the small-signal model of the hybrid GFM-GFL offshore wind farm integrated with the DRU-HVDC system can be described as:

$$\frac{\mathrm{d}\Delta \boldsymbol{x}_{\mathrm{sys}}}{\mathrm{d}t}=\boldsymbol{A}_{\mathrm{sys}}\Delta \boldsymbol{x}_{\mathrm{sys}}+\boldsymbol{B}_{\mathrm{sys}}\Delta \boldsymbol{u}_{\mathrm{sys}} \tag{13}$$

where $\boldsymbol{A}_{\mathrm{sys}}$ is the state matrix; $\boldsymbol{B}_{\mathrm{sys}}$ is the input matrix; $\Delta \boldsymbol{x}_{\mathrm{sys}}=[\Delta \boldsymbol{x}_{\mathrm{wm}i}, \Delta \boldsymbol{x}_{\mathrm{wl}i}, \Delta \boldsymbol{x}_{\mathrm{ac}i}, \Delta \boldsymbol{x}_{\mathrm{acf}}, \Delta \boldsymbol{x}_{\mathrm{dc}}]^{\mathrm{T}}$, $\Delta \boldsymbol{x}_{\mathrm{wm}i}$ and $\Delta \boldsymbol{x}_{\mathrm{wl}i}$ are the state vectors of the i^{th} GFM WT and i^{th} GFL WT, respectively, and $\Delta \boldsymbol{x}_{\mathrm{ac}i}$, $\Delta \boldsymbol{x}_{\mathrm{acf}}$, and $\Delta \boldsymbol{x}_{\mathrm{dc}}$ describe the state vectors of the i^{th} AC cable, AC filter, and HVDC system, respectively; and the input vector $\Delta \boldsymbol{u}_{\mathrm{sys}}=[\Delta P_{\mathrm{f}i}^{*}, \Delta Q_{\mathrm{f}i}^{*}, \Delta U_{\mathrm{dcw}i}^{*}, \Delta Q_{\mathrm{g}i}^{*}, \Delta U_{\mathrm{dci}}]^{\mathrm{T}}$, $\Delta P_{\mathrm{f}i}^{*}$ and $\Delta Q_{\mathrm{f}i}^{*}$ are the variations of the reference active and reactive power of the i^{th} GFM WT, respectively, $\Delta U_{\mathrm{dcw}i}^{*}$ and $\Delta Q_{\mathrm{g}i}^{*}$ are the variations of the reference DC voltage and reactive power of the i^{th} GFL WT, respectively, and U_{dci} is the variation of the DC voltage on the inverter side.

III. System Stability Analysis

The effects of the offshore reactive load, proportion of GFM WTs, and proportional coefficient of reactive power-frequency controller K_{qm} on small-signal stability are next analyzed. The corresponding operating conditions are summarized in Table I, where the power variables are per-unit values based on the installed capacity of the wind farm. Appendix A lists the system parameters, and Appendix B describes the validation of the small-signal model. To analyze the eigenvalues clearly and obtain general conclusions, the hybrid offshore wind farm is simplified into two GFM WTs and two GFL WTs with equivalent AC cables to reflect the interaction between WTs of the same and different types. Although the small-signal model is simplified, the analytical results are verified using the detailed simulation model described in Section VI, which indicates that the analytical results of the simplified model are general and can be extended to a detailed system.

TABLE I
Operating Conditions of Stability Analysis

Section	Active power of wind farm (p.u.)	Proportion of GFM WTs (%)	Reactive capacity of AC filter (p.u.)	Reactive power of all GFL WTs (p.u.)	K_{qm}
Section III-A	1	10	0.4 to 0.3	0	0.010
	1	10	0.4	0 to 0.06	0.010
Section III-B	1	90 to 10	0.4	0	0.010
	1	10 to 1	0.4	0.06	0.010
Section III-C	1	40, 10	0.4	0	0.040 to 0.004

A. Offshore Reactive Load

Two scenarios for reducing the offshore reactive load that GFM WTs must balance are studied: ① the reactive capacity of AC filter is reduced and AC cables are used to compensate for a portion of the reactive power of DRU; and ② GFL WTs compensate for the reactive power of AC cables.

First, the reactive capacity of AC filter, as a single variable, is reduced from 0.4 to 0.3 p.u. and the reactive power of GFL WTs is maintained at 0, and the root loci of dominant eigenvalues are shown in Fig. 4(a), which shows that the real part of $\lambda_{58,59}$ decreases, and real eigenvalue $\lambda_{60,61}$ becomes conjugated root and shifts left. Based on participation factors, the dominant state variable of $\lambda_{58,59}$ is the relative phase angle $\Delta\delta_{\mathrm{m2}}$ between the local reference frame of the second GFM WT and the common reference frame (i.e., the local reference frame of the first GFM WT), and $\lambda_{60,61}$ is coupled with the differential loop of the q-axis voltage controller of the GFM WTs $\Delta x_{\mathrm{u}q1,2}$. This indicates that the performance of frequency control and the synchronization of GFM WTs are advanced. Therefore, the reactive capacity of AC filter can be reduced to utilize the reactive power of AC cables and improve the system stability.

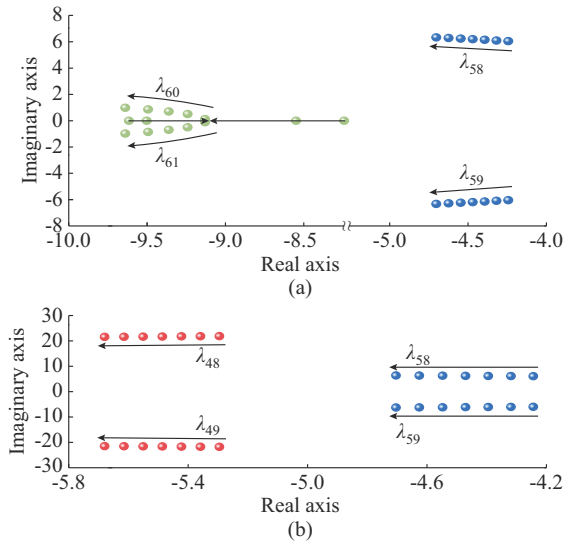

Fig. 4. Root loci of dominant eigenvalues when offshore reactive load is reduced. (a) Reactive capacity of AC filter decreases from 0.4 to 0.3 p.u.. (b) Reactive power of GFL WTs increases from 0 to 0.06 p.u..

Second, the input reactive power of GFL WTs, as a single variable, gradually increases from 0 to 0.06 p.u., and the root loci of the dominant eigenvalues are shown in Fig. 4(b). The AC filter fully compensates for the rated reactive power of DRU. The state variables highly coupled with $\lambda_{48,49}$ include the relative phase angles between local reference frames of GFL WTs and the common reference frame $\Delta\delta_{\mathrm{l1,2}}$ and differential loop in PLLs $\Delta x_{\mathrm{PLL1,2}}$. Dominant eigenvalues $\lambda_{48,49}$ and $\lambda_{58,59}$ move away from the imaginary axis, which suggests that the synchronization performance of GFM WTs is enhanced and the dynamic capability of the PLL in GFL WTs is improved. Thus, it is beneficial for GFL WTs to compensate for more unbalanced reactive power, which can not only avoid the overcurrent of GFM WTs, but also improve small-signal stability. In addition, the dominant eigenvalue $\lambda_{48,49}$ sensitive to the proportion of GFM WTs shifts left in Fig. 4(b), but not in Fig. 4(a). Therefore, as compared with reducing the capacity of AC filter, increasing the reactive power of GFL WTs can better improve the system stability under a low proportion of GFM WTs.

B. Proportion of GFM WTs

The active power of the offshore wind farm is 1 p.u., the reactive power of GFL WTs is set to be 0, and the AC filter fully compensates for the DRU. In this case, the reactive power of all the AC cables is balanced by the GFM WTs. Therefore, the proportion of GFM WTs should be at least 10% to avoid reaching the current limit of 1.2 p.u.. The ratio of the installed capacity of the GFM WTs to the total installed capacity of the offshore wind farm varies from 90% to 10%, and the root loci of the dominant eigenvalues are shown in Fig. 5(a). It shows that dominant eigenvalues $\lambda_{48,49}$ and $\lambda_{58,59}$ move toward the imaginary axis, the real parts of λ_{21}-λ_{36} increase, and $\lambda_{39,40}$ shifts right rapidly. Based on the participation factors, $\lambda_{21,22}$ and $\lambda_{25,26}$ are coupled with the *d*-axis voltage of GFM WTs $\Delta u_{\mathrm{fm}d1,2}$; $\lambda_{23,24}$ and $\lambda_{27,28}$ are coupled with the *q*-axis voltage of GFM WTs $\Delta u_{\mathrm{fm}q1,2}$; $\lambda_{29,30}$ and $\lambda_{33,34}$ are coupled with the *d*-axis voltage of GFL WTs $\Delta u_{\mathrm{fl}d1,2}$; $\lambda_{31,32}$ and $\lambda_{35,36}$ are coupled with the *q*-axis voltage of GFL WTs $\Delta u_{\mathrm{fl}q1,2}$; and $\lambda_{39,40}$ is coupled with the *d*-axis voltage at the PCC Δu_{rd}.

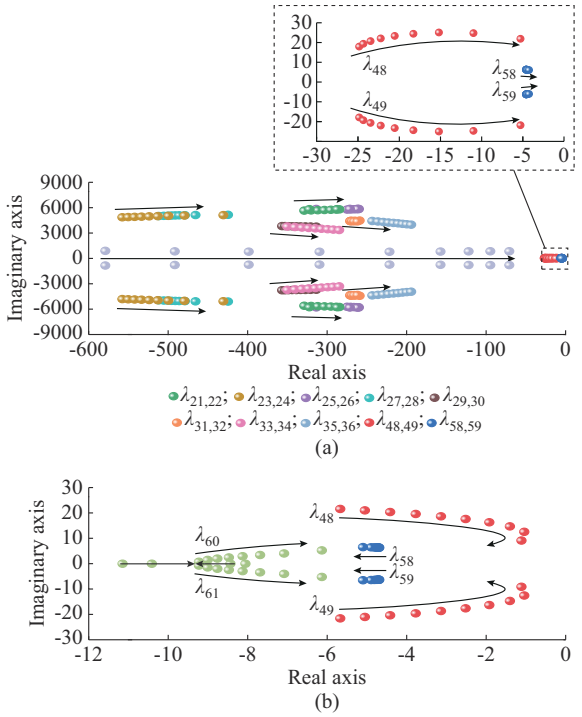

Fig. 5. Root loci of dominant eigenvalues when proportion of GFM WTs varies. (a) Proportion of GFM WTs is reduced from 90% to 10%. (b) Proportion of GFM WTs is reduced from 10% to 1% when GFL WTs fully compensate reactive power of AC cables.

When the GFM WTs are reduced, the sensitive eigenvalues move right without reaching the right plane, indicating that system damping is reduced while the small-signal stability is maintained. Three trends in the small-signal stability can be observed. ① Eigenvalues related to the *d*- and *q*-axis voltages of GFM WTs shift right, reflecting the weakened AC voltage amplitude and frequency control performance of GFM WTs. ② The reactive power of each GFM WT increases, causing a greater frequency deviation; at this point, the self-synchronization performance of GFM WTs deteriorates. ③ The dynamic capability of PLL in GFL WTs worsens. Thus, with insufficient GFM WTs, the parameters of PLL, voltage controllers of GFL WTs, and reactive power-frequency and voltage controllers of GFM WTs should be optimized.

If the reactive power of AC cables is fully compensated by the GFL WTs, the question remains as to whether the proportion of the GFM WTs can be further reduced. When the penetration of the GFM WTs is reduced from 10% to 1%, no overcurrent occurs during the process. As Fig. 5(b) shows, the real eigenvalue $\lambda_{60,61}$ becomes conjugated root and shifts right, and $\lambda_{48,49}$ approaches the imaginary axis but always in the left plane. Thus, under the rated condition, if the reactive power of AC cables is fully compensated by GFL WTs, the system remains small-signal stable even if the proportion of GFM WTs decreases to 1%. In other words, as long as the GFM WTs experience no current saturation and retain their GFM capabilities, a single GFM WT serving as the AC voltage source can support a large-capacity hybrid GFM-GFL offshore wind farm integrated with DRU-HVDC system.

C. Proportional Coefficient of Reactive Power-frequency Controller

The reactive power-frequency controller of GFM WTs is critical in supporting offshore frequency and maintaining the reactive power balance. The proportional coefficient of reactive power-frequency controller K_{qm} declines from 0.040 to 0.004, and the root loci of dominant eigenvalues are plotted in Fig. 6. With a decrease in K_{qm}, $\lambda_{58,59}$ moves significantly toward the imaginary axis, indicating worse synchronization performance between GFM WTs. $\lambda_{48,49}$ is also close to the imaginary axis with a small K_{qm} when the proportion of GFM WTs is reduced.

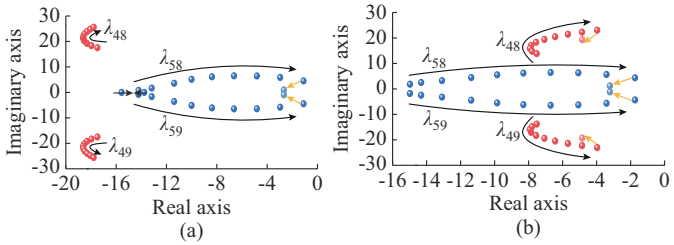

Fig. 6. Root loci of dominant eigenvalues when K_{qm} is reduced from 0.040 to 0.004 with different proportions of GFM WTs. (a) Proportion of GFM WTs is 40%. (b) Proportion of GFM WTs is 10%.

Selecting a smaller K_{qm} is preferable to reduce the frequency deviation. However, the stability analysis results indicate that a smaller K_{qm} leads to a reduced system damping. To satisfy the steady-state frequency error and improve the system dynamic response, an additional compensator is designed for the reactive power-frequency controller of GFM WTs.

First, K_{qm} is determined to satisfy the steady-state frequency error requirement. Setting K_{qm} to be 0.004 to achieve a 1.0 p.u. reactive power change of GFM WTs results in an offshore frequency deviation of only 0.004 p.u.. Based on the developed small-signal model, Fig. 7(a) shows the frequency-domain Bode response of the original open-loop system under the reactive power-frequency proportional control. The

reactive power-frequency control loop of the GFM WT is positive feedback, and the phase margin (PM) at the crossover frequency ω_{PM} is 77.1°, which determines damping and overshoot. To improve the system damping, the PM should be increased, and the phase lead θ_{lead} can be set to be 40° as an example. The lead compensator is designed to alter the open-loop phase as:

$$D(s)=\frac{s\mathcal{T}+1}{s\beta\mathcal{T}+1} \tag{14}$$

where β and $\mathcal{T}$ are the zero and pole time constants, respectively, which are calculated as:

$$\beta=\frac{1-\sin\theta_{lead}}{1+\sin\theta_{lead}} \tag{15}$$

$$\mathcal{T}=\frac{1}{\omega_{PM}\sqrt{\beta}} \tag{16}$$

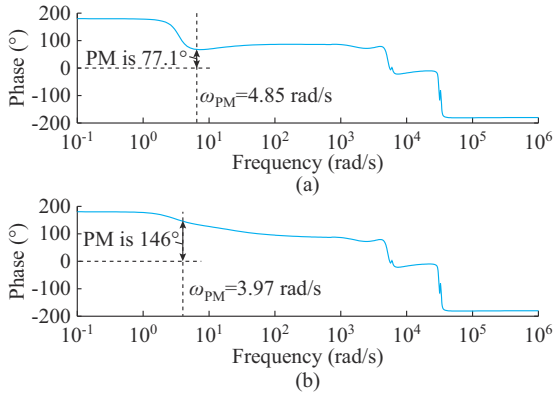

Fig. 7. Frequency-domain Bode response. (a) Original open-loop system. (b) Compensated system.

Figure 8 shows the reactive power-frequency compensation control of GFM WTs. According to the Bode response shown in Fig. 7(b), the PM of the compensated system is improved. In addition, the dominant eigenvalues of the compensated system shift left, as shown by the yellow arrows in Fig. 6, indicating higher damping and lower overshoot with a small frequency deviation.

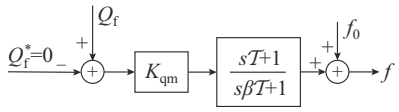

Fig. 8. Reactive power-frequency compensation control of GFM WTs.

IV. Offshore Reactive Power Optimization

A. Prerequisite for GFM Capability

Effective GFM capabilities of WTs are essential to the normal operation of the hybrid GFM-GFL offshore wind farm integrated with the DRU-HVDC system. To avoid the overcurrent, the reference current of WT controller is limited by using a hard limiter, as illustrated in Fig. 2. Depending on whether the reference current reaches the limit, the control characteristics of GFM WT can be divided into two situations: ① if the reference current does not reach the limit and is generated by the GFM strategy, the GFM WT can be considered an AC voltage source with controllable voltage amplitude and frequency; ② once the reference current is equal to the limit and is no longer generated by the GFM strategy, the GFM WT becomes a constant current source without AC voltage control ability.

Therefore, the basic prerequisite for GFM WTs in effectively supporting offshore AC voltage is that they should not enter the current saturation state. The steady-state current of the GFM WT incorporates both active and reactive components. Under the MPPT algorithm, the wind speed determines the active current. For the reactive current, GFM WTs serve as reactive power balancing nodes in the hybrid GFM-GFL offshore wind farm integrated with the DRU-HVDC system, which automatically and uniformly perform the reactive power balancing task. If insufficient GFM WTs must balance the large offshore reactive load, the steady-state current saturation of GFM WTs may occur.

B. Variations in Offshore Reactive Power

The reactive load in a hybrid GFM-GFL offshore wind farm integrated with the DRU-HVDC system mainly includes two aspects: ① the DRU and converter transformer require plenty of inductive reactive power, which should be compensated by a passive AC filter parallel to the PCC; ② numerous AC cables absorb capacitive reactive power, which is approximately 60 Mvar in a 1000 MW offshore wind farm [41]. The on-load and no-load reactive power of the capacitive AC cables may be not very diverse. Thus, the major offshore reactive load Q_{load} is expressed as:

$$Q_{load}=Q_{cable}+Q_{filter}-Q_r \tag{17}$$

where Q_{cable} and Q_{filter} are the reactive power of AC cables and AC filter, respectively.

The DC voltage of DRU U_{dcr} can be considered constant as U_{const} controlled by the MMC inverter. According to (7), the DC current of DRU satisfies:

$$I_{dcr}=\left(\frac{6\sqrt{2}}{\pi T}U_r-U_{const}\right)\Big/\left(\frac{6X_{tr}}{\pi}\right) \tag{18}$$

Based on (12) and (18), the active power of DRU P_r can be derived as:

$$P_r=U_{dcr}I_{dcr}=\frac{\sqrt{2}\,U_{const}}{TX_{tr}}U_r-\frac{\pi U_{const}^2}{6X_{tr}} \tag{19}$$

It can be observed that the DC current I_{dcr} and PCC voltage U_r are determined by the transmitted active power P_r. By substituting (19) into (11), we can replace the variables I_{dcr} and U_r in (11) with P_r. Thus, the overlap angle μ of DRU is rewritten as:

$$\mu=\arccos\left(1-\frac{2X_{tr}P_r}{X_{tr}P_r+\pi U_{const}^2/6}\right) \tag{20}$$

According to (10) and (20), the absorbed reactive power of DRU Q_r is determined by its transmitted active power P_r, as plotted in Fig. 9. All the power variables shown in Fig. 9 are per-unit values based on the installed capacity of the offshore wind farm. As shown in Fig. 9, Q_r is 0.394 p.u. under the rated active power condition in the case system. When

P_r is reduced to 0.1 p.u., Q_r decreases to 0.0123 p.u., and the ratio of Q_r to P_r decreases. The offshore AC filter groups cannot be switched frequently with wind speed fluctuations. If the reactive capacity of AC filter is configured according to the rated reactive power demand of DRU under the rated active power condition (i.e., Q_{filter} is 0.4 p.u.), excess reactive power will be generated by the AC filter when the DRU transmits less active power. This in turn causes the offshore reactive load Q_{load} to increase from 0.0656 to 0.448 p.u..

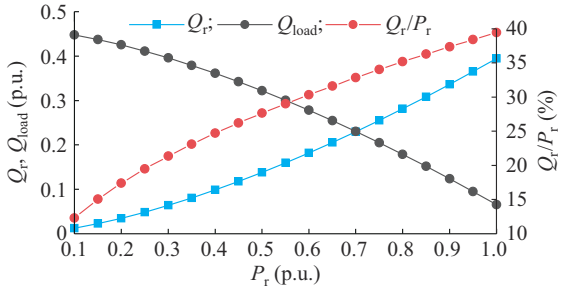

Fig. 9. Curves of Q_r, Q_{load}, and ratio of Q_r to P_r over full active power range.

C. Offshore Reactive Power Optimization Methods

To diminish the offshore reactive power imbalance that GFM WTs must control and avoid the current saturation of low-proportion GFM WTs in the hybrid GFM-GFL wind farm integrated with the DRU-HVDC system, two offshore reactive power optimization methods are proposed.

A passive method is to employ an optimal design for the reactive capacity of the filter, which can be done in two steps. First, because the capacitive reactive power of AC cables can be utilized to offset a portion of the inductive reactive power of the DRU, the AC filter and AC cables are configured to jointly provide reactive power compensation to the DRU. Second, because WTs have output reactive power capabilities, the AC filter and AC cables do not need to fully compensate for the rated reactive power of the DRU. Thus, the reactive capacity of AC filter can be further reduced to the minimum filtering capacity, which is defined as the minimum capacity that ensures the harmonic distortion of the PCC voltage is below the harmonic distortion limit under IEEE Standard 519 over the full active power range.

Compared with the AC filter generally configured to fully compensate the rated reactive power of the DRU (approximately 0.4 p.u., as plotted in Fig. 9), the optimal capacity of AC filter can be reduced to 0.3 p. u. in the case system. Thus, the excess reactive power of AC filter under low wind power can be reduced, thereby diminishing the offshore reactive power balancing burden of low-proportion GFM WTs. In addition, the AC filter has a significant impact on the cost of an offshore DRU platform, and its optimal capacity can reduce the volume and weight of AC filter and further improve the economy of the offshore DRU platform.

An active method is to achieve the dynamic reactive power compensation using GFL WTs. The GSC of GFL WT can actively adjust the output reactive power. To evenly distribute the reactive load among all GFL WTs based on their installed capacities, the per-unit reference reactive power of each GFL WT Q^*_{wl} is set as:

$$Q^*_{wl} = \frac{K_{qwl} Q_{load} P_{wfN}}{\sum P_{wlNi}} = \frac{K_{qwl} Q_{load}}{1 - K_{wm}} \tag{21}$$

where P_{wlNi} is the installed capacity, i.e., rated active power, of the i^{th} GFL WT; K_{wm} is the ratio of the installed capacity of GFM WTs to the installed capacity of offshore wind farm P_{wfN}; and K_{qwl} is the ratio of the reactive load that is expected to be compensated by GFL WTs to the total reactive load. The offshore reactive load Q_{load} is calculated based on the active power of DRU P_r.

The reference current of GFL WT controller is also limited by a hard limiter to avoid overcurrent. When the proportion of GFM WTs is low, a sufficient number of GFL WTs participate in reactive power compensation without current saturation. However, as the proportion of GFM WTs increases, the reactive power of each GFL WT also increases. To prevent GFL WTs from reaching current saturation, the maximum reference reactive power Q^*_{wlmax} is defined as:

$$Q^*_{wlmax} = \sqrt{I^2_{limit} - (P^*_{wl})^2} \tag{22}$$

where P^*_{wl} is the per-unit reference active power of each GFL WT.

Based on (21) and (22), the reactive power compensation control loop of GFL WTs is illustrated in Fig. 10. Compare the absolute values of Q^*_{wl} and Q^*_{wlmax}, and select the smaller value as the reference reactive power for GFL WT. The reference reactive power is fed into the q-axis outer-loop controller for the GSC of GFL WT to generate the q-axis reference current [40]. The red and blue arrows indicate the changes in the power variables as P_r increases and decreases, respectively. Thus, the GFL WTs can dynamically compensate for the offshore reactive load and share the reactive power balancing task of low-proportion GFM WTs.

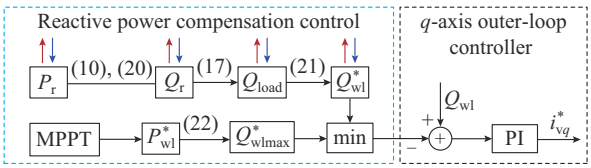

Fig. 10. Reactive power compensation control loop of GFL WTs.

V. Determining Proportion of GFM WTs

A. Principle and Calculation Method for Determining Proportion of GFM WTs

The principle for determining the proportion of GFM WTs is analyzed considering the system stability and optimal offshore reactive power constraints as follows. The eigenvalue analysis results reveal that a very low proportion of GFM WTs can maintain system stability as long as GFM WTs do not enter current saturation. Thus, the small-signal stability is not the dominant factor affecting the proportion of GFM WTs. Based on the reactive load analysis results, GFM WTs must undertake the offshore reactive power balancing task because of the reactive characteristics of DRU. Thus, insufficient GFM WTs may experience steady-state current saturation and lose their effective GFM capabilities. Therefore, the

principle for determining the proportion of GFM WTs is that no current saturation occurs in the GFM WTs under various steady-state conditions, and a certain margin between the reference current and its limit should be considered.

Determining the proportion of GFM WTs by simulation and examining all steady-state conditions are complicated. A calculation method is proposed for quickly determining the proportion of GFM WTs while considering various steady-state conditions and reactive power optimization. GFM WTs equally share unbalanced offshore reactive power by reactive power-frequency control. Therefore, the per-unit reactive power of each GFM WT Q_{wm} can be expressed as:

$$Q_{wm}=\frac{Q_{load}P_{wfN}}{\sum P_{wmNi}}=\frac{Q_{load}}{K_{opm}K_{wm}} \tag{23}$$

where P_{wmNi} is the installed capacity of the i^{th} GFM WT in operation; and K_{opm} is the operational rate of GFM WTs, which is the ratio of the installed capacities of GFM WTs in operation to those of all GFM and GFL WTs.

Based on (23), the apparent power of GFM WT S_{wm} satisfies:

$$S_{wm}=\sqrt{P_{wm}^2+Q_{wm}^2}=\sqrt{P_{wm}^2+\left(\frac{Q_{load}}{K_{opm}K_{wm}}\right)^2} \tag{24}$$

where P_{wm} is the per-unit active power of each GFM WT.

Here, S_{wm} increases as K_{wm} decreases. The per-unit value of S_{wm} is approximately equal to the current amplitude reference I_v^* because the WT voltage amplitude is approximately 1 p.u. in the steady state. To avoid the overcurrent of GFM WTs, a critical proportion $K_{wm,cr}$ exists when S_{wm} reaches the current limit I_{limit}. Based on (24), the critical proportion of GFM WTs $K_{wm,cr}$ is defined as:

$$K_{wm,cr}=\sqrt{\frac{Q_{load}^2}{K_{opm}^2(I_{limit}^2-P_{wm}^2)}} \tag{25}$$

Here, $K_{wm,cr}$ is determined by P_{wm}, the operational rate of GFM WTs K_{opm}, and the offshore reactive load Q_{load}. Based on (10), (17), and (20), the offshore reactive load Q_{load} primarily changes with the transmitted active power P_r, which is affected by P_{WM}, K_{opm}, and the operational rate of GFL WTs K_{opl}. Therefore, the critical proportion $K_{wm,cr}$ of GFM WTs is related to P_{wm}, K_{opm}, K_{opl}, and Q_{load}. By changing these variables, we can determine the critical proportion of GFM WTs when considering the full active power range and offshore reactive power optimization.

B. Critical Proportion of GFM WTs over Full Active Power Range

The per-unit active power of all WTs is set to be equal. The active power variation of GFM WTs from 0.1 to 1.0 p.u., caused by wind speed fluctuations, is first considered. Based on (23) and (25), the reactive power and critical proportion of the GFM WTs, i.e., Q_{wm} and $K_{wm,cr}$, are calculated, respectively, as shown in Fig. 11. The decline in the active power of wind farm leads to a decrease in the transmitted active power and absorbed reactive power of DRU. To absorb a large amount of excess reactive power from the AC filter, $K_{wm,cr}$ increases to 37.4% to avoid the overcurrent of GFM WTs over the full active power range.

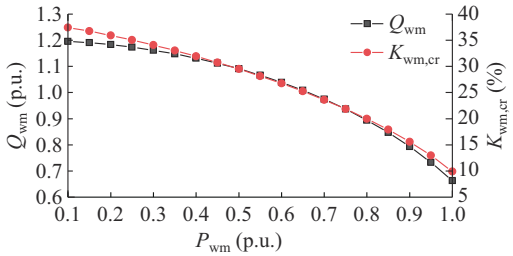

Fig. 11. Curves of Q_{wm} and $K_{wm,cr}$ over full active power range.

The outage of partial WTs also significantly affects the active power of wind farm. When wind speed fluctuations are simultaneously considered, the operational rates of GFL WTs and GFM WTs K_{opl} and K_{opm} are reduced from 100% to 50% in sequence, and the critical proportions of GFM WTs $K_{wm,cr}$ are illustrated in Fig. 12. The outage of partial WTs decreases the transmitted active power and absorbed reactive power of DRU. To absorb more excess reactive power from the AC filter, $K_{wm,cr}$ increases. A comparison of Fig. 11 and Fig. 12(a) shows that, because all GFM WTs are in operation and uniformly withstand the reactive load, $K_{wm,cr}$ is not significantly affected by the partial outage of GFL WTs. However, if some GFM WTs are cut off, the reactive power borne by each remaining GFM WT increases as the reciprocal of K_{opm}. Under these circumstances, the critical proportion of GFM WTs increases rapidly to 91.6% when only half of GFM WTs are in operation, as shown in Fig. 12(b). Accordingly, the outage of partial GFM WTs should be avoided in the hybrid GFM-GFL offshore wind farm integrated with the DRU-HVDC system. If numerous GFM WTs are shut down, the corresponding number of AC filter groups should be cut off to diminish the offshore reactive power imbalance.

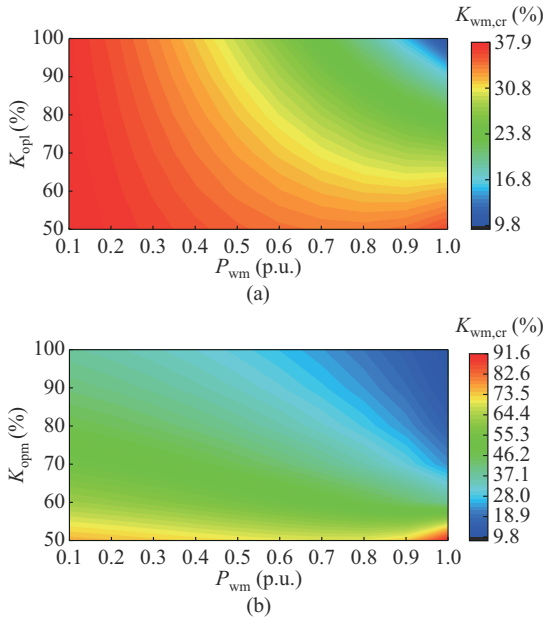

Fig. 12. Critical proportions of GFM WTs $K_{wm,cr}$ over full active power range with different K_{opl} and K_{opm}. (a) K_{opl} is reduced from 100% to 50%. (b) K_{opm} is reduced from 100% to 50%.

C. Critical Proportion of GFM WTs Under Reactive Power Optimization

Offshore reactive power optimization methods have been proposed to reduce the offshore reactive power imbalance. The effect of reactive power optimization on the critical proportion of the GFM WTs is analyzed as follows.

The reactive capacity of AC filter Q_{filter} decreases from 0.4 to 0.3 p.u., which in turn reduces the excess reactive power of the AC filter and the reactive power balancing pressure of the GFM WTs. Consequently, $K_{\text{wm,cr}}$ decreases gradually with a decrease in Q_{filter} over the full active power range, as illustrated in Fig. 13(a). However, the reactive power optimization effect based on passive devices is limited, and a large reactive power imbalance still exists when the active power of wind farm is low. Therefore, $K_{\text{wm,cr}}$ is reduced only to 29.1% when Q_{filter} is 0.3 p.u..

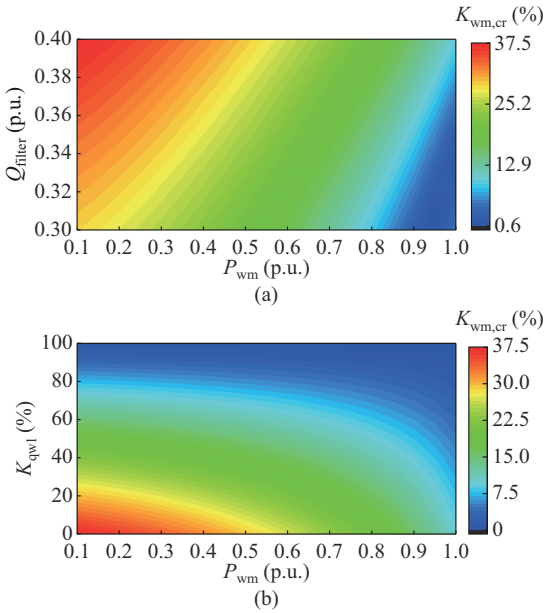

Fig. 13. Critical proportions of GFM WTs $K_{\text{wm,cr}}$ over full active power range with different Q_{filter} and K_{qwl}. (a) Q_{filter} is reduced from 0.4 to 0.3 p.u.. (b) K_{qwl} is increased from 0% to 100%.

By adopting the reactive power compensation control, GFL WTs can dynamically compensate the offshore reactive load and share the reactive power balancing task of low-proportion GFM WTs. When GFL WTs consume more reactive power as K_{qwl} increases from 0% to 100%, $K_{\text{wm,cr}}$ can be significantly reduced, as shown in Fig. 13(b). When K_{qwl} is set to be 100%, the changing offshore reactive load can be compensated by GFL WTs. At this time, few GFM WTs only need to balance the remaining small amount of reactive power and are less likely to experience overcurrent.

VI. Case Study

A. System Configuration

To verify the theoretical analysis results of the hybrid GFM-GFL offshore wind farm integrated with the DRU-HVDC system and the effectiveness of the proposed determination method for the proportion of GFM WTs and reactive power optimization methods, a detailed model shown in Fig. 14 is established using PSCAD/EMTDC. Based on practical offshore wind projects, the rated power of each WT is selected to be 10 MW, and each WT cluster includes five WTs connected in series through practical 66 kV submarine cables. Twenty WT clusters are contained in the 1000 MW wind farm. The proportion of GFM WTs can be altered by changing the number of GFM WT clusters. Appendix A lists the main circuit parameters of this model.

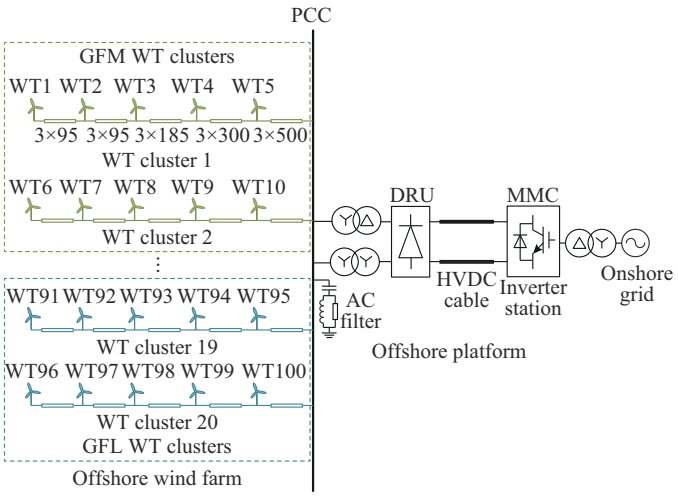

Fig. 14. Detailed model of case system.

B. Simulation Verification

According to Fig. 11, when P_{wm} is 0.1 p.u. and 1.0 p.u., the critical proportions of GFM WTs $K_{\text{wm,cr}}$ are calculated as 37.4% and 9.89%, respectively. To verify the calculation results for the proportion of GFM WTs, cases with different numbers of GFM WT clusters are simulated, as listed in Table II. The per-unit power variables listed in Table II are based on the installed capacity of wind farm.

TABLE II
Simulation Cases Under Different Numbers of GFM WT Clusters

Case	P_{WM} (p.u.)	Proportion (%)		Number of WT clusters		Reactive capacity of AC filter (p.u.)	Reactive power of all GFL WTs (p.u.)
		GFM WT	GFL WT	GFM WT	GFL WT		
1	0.1	40	60	8	12	0.4	0
2	0.1	35	65	7	13	0.4	0
3	1.0	10	90	2	18	0.4	0
4	1.0	5	95	1	19	0.4	0
5	1.0	5	95	1	19	0.3	0
6	1.0	5	95	1	19	0.4	0.06

As shown in Figs. 15 and 16, when the proportions of GFM WTs in Cases 1 and 3 are greater than the calculated $K_{\text{wm,cr}}$, the offshore AC voltage can be controlled by the GFM WTs, and the large-capacity DRU-based offshore wind integration system can operate stably. However, in Cases 2 and 4, as illustrated in Fig. 17, insufficient GFM WTs need to balance large reactive load and may reach current saturation. At this time, the output AC voltages of GFM WTs can-

not be controlled effectively, and they may experience oscillatory instability. Therefore, the calculated $K_{wm,cr}$ is validated, and the proportion of GFM WTs should be greater than 37.4% under a margin that considers the entire wind power fluctuation range.

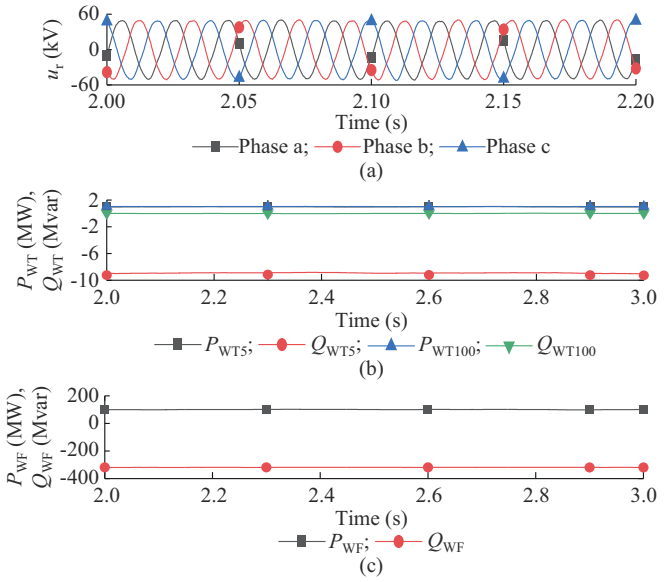

Fig. 15. Steady-state simulation results in Case 1. (a) u_r. (b) Active and reactive power of WT5 and WT100. (c) Active and reactive power of wind farm.

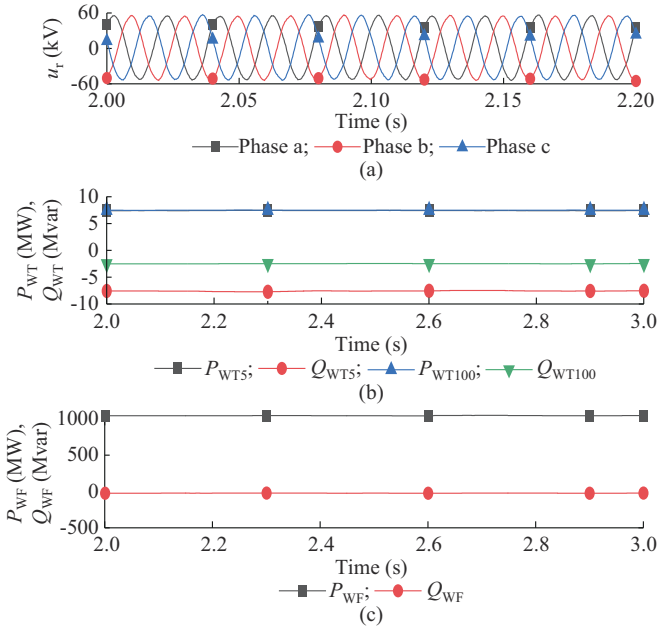

Fig. 16. Steady-state simulation results in Case 3. (a) u_r. (b) Active and reactive power of WT5 and WT100. (c) Active and reactive power of wind farm.

If the active power of wind farm in Case 1 is set to be 1.0 p.u., the proportion of GFM WTs becomes a single variable in Cases 1 and 3. The systems in the two cases operate stably under the rated active power condition before $t=2.0$ s, as shown in Figs. 18 and 19. At $t=2.0$ s, the reference reactive power of GFL WTs has a step change, causing the total input reactive power of GFL WTs to change from 0 to −120 Mvar. At this time, the reactive power of GFM WTs under reactive power-frequency control is automatically changed to maintain the offshore reactive power balance. This means that when the GFM WTs are reduced, the responses of the reactive power and frequency become more oscillatory, indicating that the system damping has weakened.

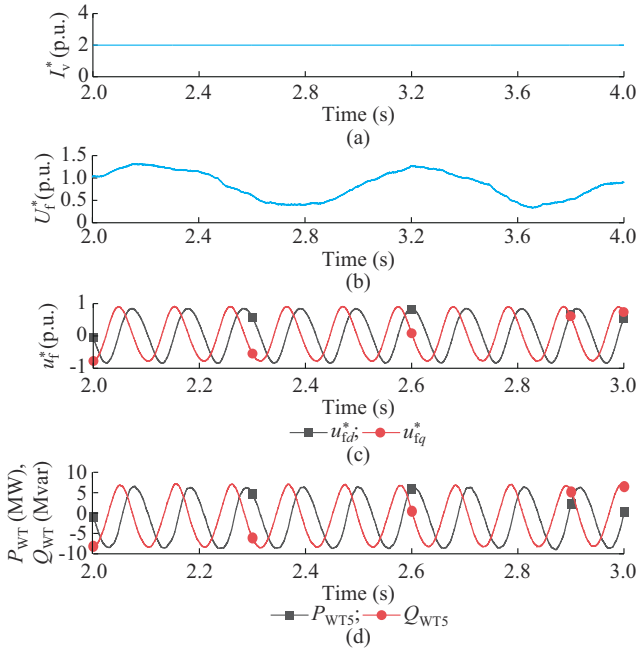

Fig. 17. Instability conditions of WT5 in Cases 2 and 4. (a) I_v^* in Cases 2 and 4. (b) U_f^* in Case 2. (c) u_f^* in Case 4. (d) Active and reactive power of WT5 in Case 4.

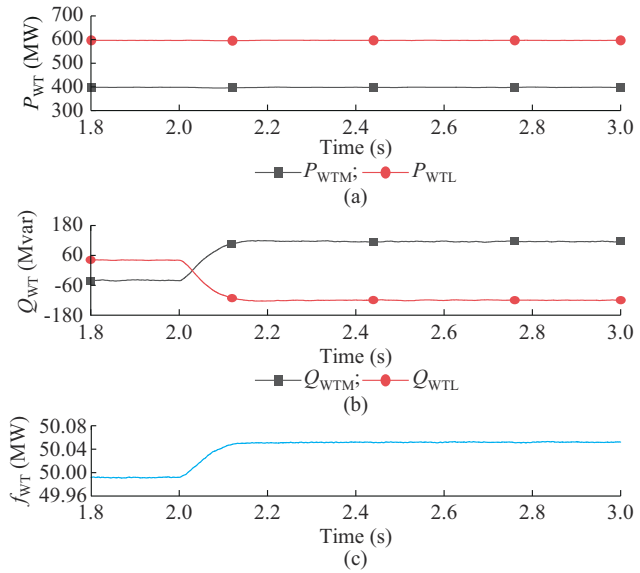

Fig. 18. Responses to step change of reactive power in Case 1. (a) Total active power of GFM and GFL WTs. (b) Total reactive power of GFM and GFL WTs. (c) Frequency of WT.

The proportion of GFM WTs is limited by possible current saturation. To avoid reactive current overload with the low proportion of GFM WTs, the effectiveness of the following two reactive power optimization methods is verified.

First, the AC filter and AC cables are set to jointly compensate the full reactive power of DRU in Case 5. Second, the GFL WTs consume all of the reactive power of AC cables in Case 6. The steady-state simulation results in Cases 5 and 6 are shown in Figs. 20 and 21, respectively. Compared with Fig. 17, if the GFM WTs do not reach current saturation under the proposed offshore reactive power optimization methods, the large-capacity DRU-based offshore wind integration system can operate stably even if only one GFM WT cluster exists.

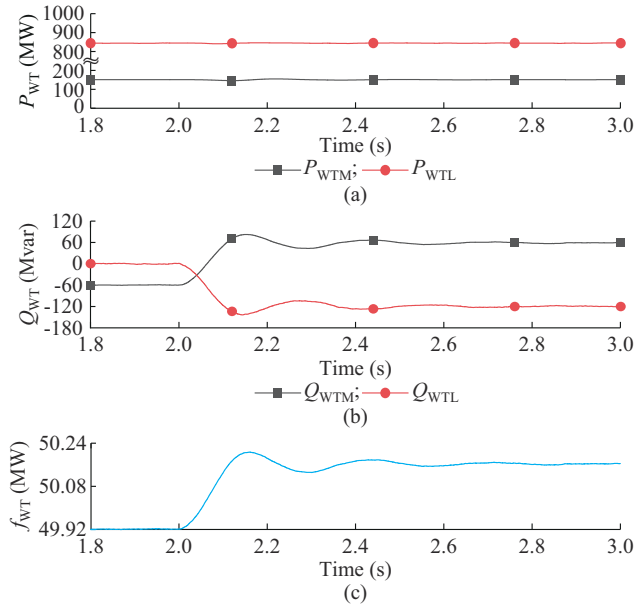

Fig. 19. Responses to step change of reactive power in Case 3. (a) Total active power of GFM and GFL WTs. (b) Total reactive power of GFM and GFL WTs. (c) Frequency of WT.

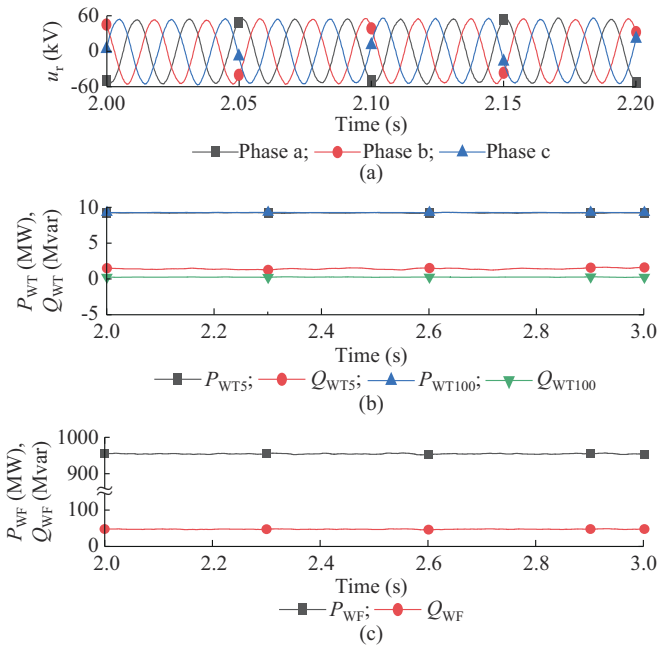

Fig. 20. Steady-state simulation results in Case 5. (a) u_r. (b) Active and reactive power of WT5 and WT100. (c) Active and reactive power of wind farm.

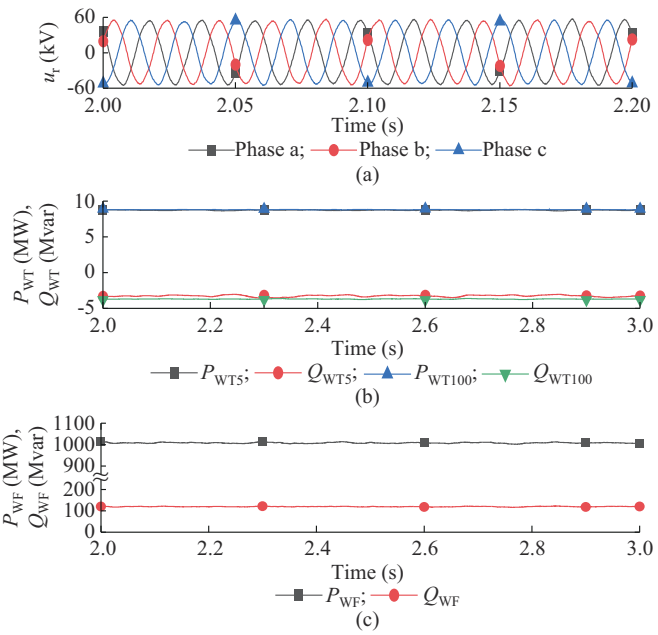

Fig. 21. Steady-state simulation results in Case 6. (a) u_r. (b) Active and reactive power of WT5 and WT100. (c) Active and reactive power of wind farm.

To verify the effects of the proportional coefficient of reactive power-frequency controller K_{qm}, we set K_{qm} in Case 3 to change from 0.040 to 0.004. The reference reactive power of the GFL WTs has a step change at $t=2.0$ s, causing the total input reactive power of GFL WTs to increase from 0 to 120 Mvar, as shown in Fig. 22. Under the reactive power-frequency proportional control, the offshore frequency increases as the reactive power of GFM WTs increases, and the frequency deviation decreases with a lower K_{qm}. During the dynamic process, a reduction in K_{qm} can lead to poorer damping and a higher overshoot of reactive power and frequency performance, and obvious oscillation will occur because of insufficient K_{qm}. To test the effectiveness of the reactive power-frequency compensation control of GFM WTs, the additional compensator is adopted at $K_{qm}=0.004$. As Fig. 22(d) shows, the overshoot of reactive power is reduced, and the oscillation is stabilized faster. This shows that the proposed reactive power-frequency compensation control for GFM WTs can suppress oscillations with lower frequency deviations.

To verify the effectiveness of the additional reactive power compensation control of GFL WTs, simulation results of the active power change caused by wind speed fluctuations are illustrated in Fig. 23. At $t=2.0$ s, as the wind speed decreases, the active power of WTs gradually decreases by half under MPPT control. Based on the active power-voltage control of GFM WTs, the output AC voltage amplitude of GFM WTs decreases, resulting in a decrease in the PCC voltage. Based on the relationship between the AC and DC voltages of DRU in (7), the DC voltage of DRU decreases slightly. Thus, the DC current and DC power of the HVDC system are both reduced, and the system smoothly enters a new stable operating point. A time delay of 100 ms is considered for the reactive power compensation controller. Based on

their reactive power compensation control, GFL WTs can dynamically consume offshore reactive power imbalances under varying active wind power. Accordingly, the reactive power of GFM WT is always low, and a small proportion of GFM WTs will not experience current saturation.

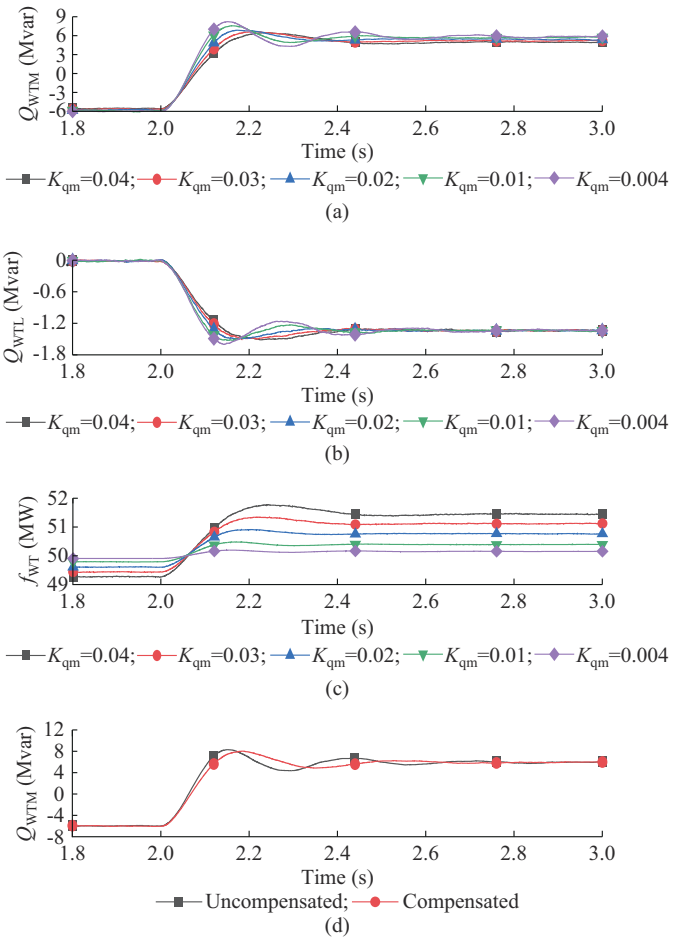

Fig. 22. Responses to reactive power step change under different K_{qm}. (a) Reactive power of a single GFM WT. (b) Reactive power of a single GFL WT. (c) Frequency of WT. (d) Reactive power of a single GFM WT with and without compensation control.

VII. Conclusion

This study proposes a method for determining the proportion of GFM WTs in a hybrid GFM-GFL offshore wind farm integrated with the DRU-HVDC system that considers system stability and optimal reactive power constraints. Three main studies are conducted: system stability is analyzed, the offshore reactive power optimization methods are proposed, and the proportion of GFM WTs is determined. The conclusions can be summarized as follows.

1) The small-signal stability is not the dominant factor affecting the proportion of GFM WTs. The system stability is improved by reducing the reactive load. A smaller reactive power-frequency coefficient leads to a lower frequency deviation but weakens the stability. The reactive power-frequency compensation control of GFM WTs is designed to improve dynamic responses and satisfy the steady-state frequency error.

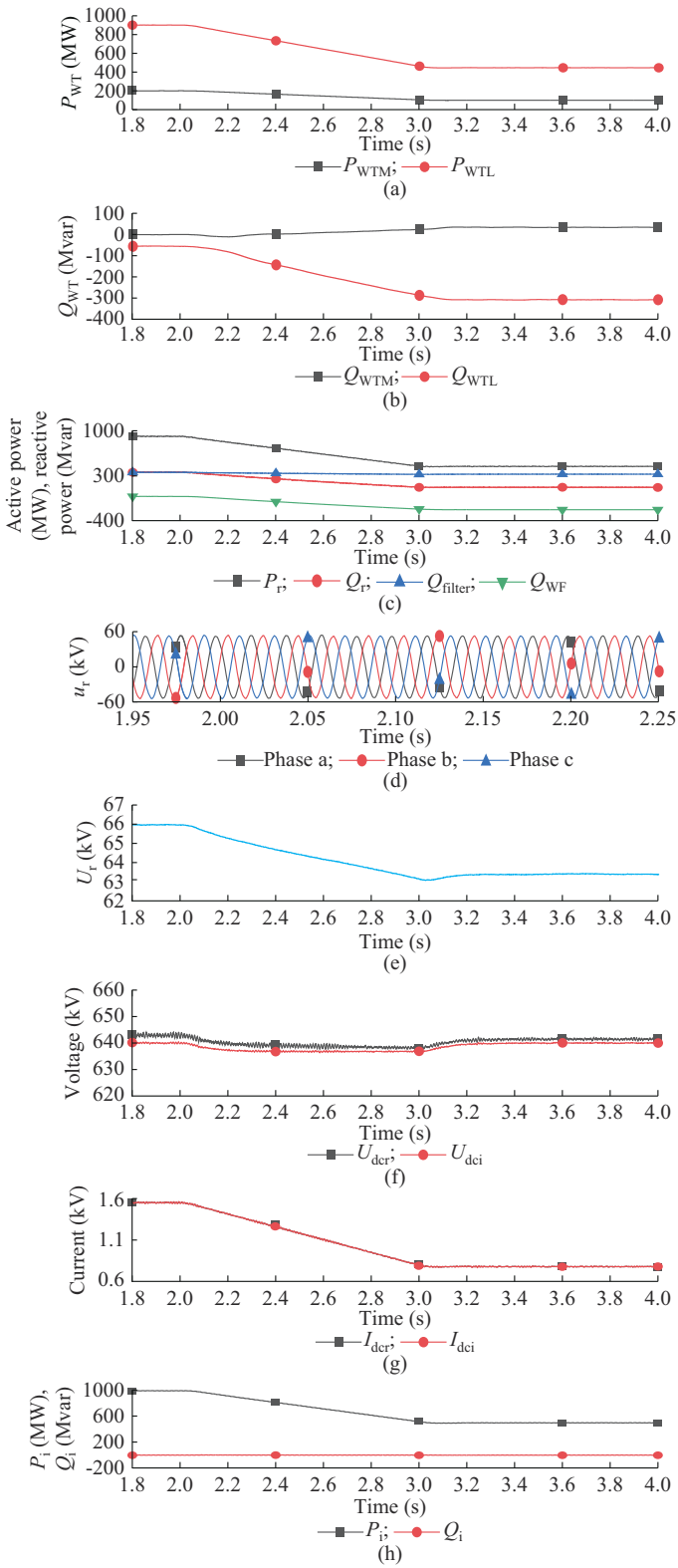

Fig. 23. Responses to active power change. (a) Active power of GFM and GFL WTs. (b) Reactive power of GFM and GFL WTs. (c) P_r, Q_{WF}, Q_r, and Q_{filter}. (d) u_r. (e) U_r. (f) DC voltage. (g) DC current. (h) Active and reactive power of MMC.

2) The offshore reactive load may cause a low proportion of GFM WTs to lose their GFM capabilities. To diminish the reactive imbalance, an offshore reactive power compensation method of GFL WTs is proposed. An optimal design for the

reactive capacity of AC filter is also proposed based on the reactive compensation capabilities of AC cables and the minimum filtering capacity. These reactive power optimization methods can avoid the overcurrent of GFM WTs, reduce the proportion of GFM WTs, and improve system stability.

3) The principle that determines the proportion of GFM WTs is that no GFM WT enters current saturation under various steady-state conditions. If the GFL WTs provide no reactive power and the AC filter compensates for the rated reactive power of DRU, the critical proportion of GFM WTs increases to 37.4% over the full active power range. When the reactive capacity of AC filter is reduced from 0.4 to 0.3 p.u., the critical proportion of GFM WTs decreases to 29.1%. If the reactive load is dynamically compensated for by GFL WTs, the proportion of GFM WTs can be significantly reduced.

APPENDIX A

TABLE AI
MAIN CIRCUIT PARAMETERS

Item	Parameter	Value
WT	Total installed capacity	1000 MW
	Rated power of single WT	10 MW
	Transformer ratio	0.69 kV/66 kV
	Transformer leakage inductance	0.07 p.u.
	Filter capacitor	0.1 p.u.
	Filter inductor	0.15 p.u.
	Steady-state current hard limit	1.2 p.u.
DRU station	Transformer rated capacity	2×550 MVA
	Transformer ratio	66 kV/258 kV
	Transformer leakage inductance	0.15 p.u.
	Reactive capacity of AC filter	400 Mvar
	Smoothing inductance	100 mH
DC cable	Line resistance	7.56 mΩ/km
	Line inductance	0.23 mH/km
	Line capacitance	0.181 μF/km
	Cable length	120 km
MMC inverter	Transformer rated capacity	1100 MVA
	Transformer ratio	500 kV/320 kV
	Transformer leakage inductance	0.1 p.u.
	Rated DC voltage	±320 kV
	Submodules per arm	350
	Submodule capacitor	11.4 mF
	Arm inductor	77.8 mH

TABLE AII
PARAMETERS OF AC SUBMARINE CABLES

Type	Line resistance ($\Omega\cdot km^{-1}$)	Line inductance ($mH\cdot km^{-1}$)	Line capacitance ($\mu F\cdot km^{-1}$)	Cable length (km)
3×95	0.1970	0.471	0.107	1
3×185	0.1040	0.425	0.131	1
3×300	0.0665	0.393	0.155	1
3×500	0.0407	0.374	0.166	10

TABLE AIII
PARAMETERS OF CONTROLLERS OF GFM WT AND GFL WT

WT	Controller	Parameter	Value
GFM WT	Active/reactive power controller	K_p	0.5
		T_p	33.33
		K_{qm}	0.01
	Voltage controller	K_v	2
		T_v	20
	Current controller	K_{cm}	1.1
		T_{cm}	20
GFL WT	Outer-loop controller	K_{dc}	5
		T_{dc}	100
		K_{qg}	0.21
		T_{qg}	34.48
	Inner-loop controller	K_{cl}	3.2
		T_{cl}	20
	PLL	K_{PLL}	50
		T_{PLL}	900

APPENDIX B

To validate the small-signal model, the step responses of the developed small-signal model in MATLAB are compared with the time-domain simulation results of the non-linear model in PSCAD/EMTDC. As plotted in Fig. B1, when the reference power of GFM WTs and GFL WTs have step changes, the performances of the small-signal model are in good agreement with the simulation results, which demonstrate the adequacy of the developed linearized model for stability analysis.

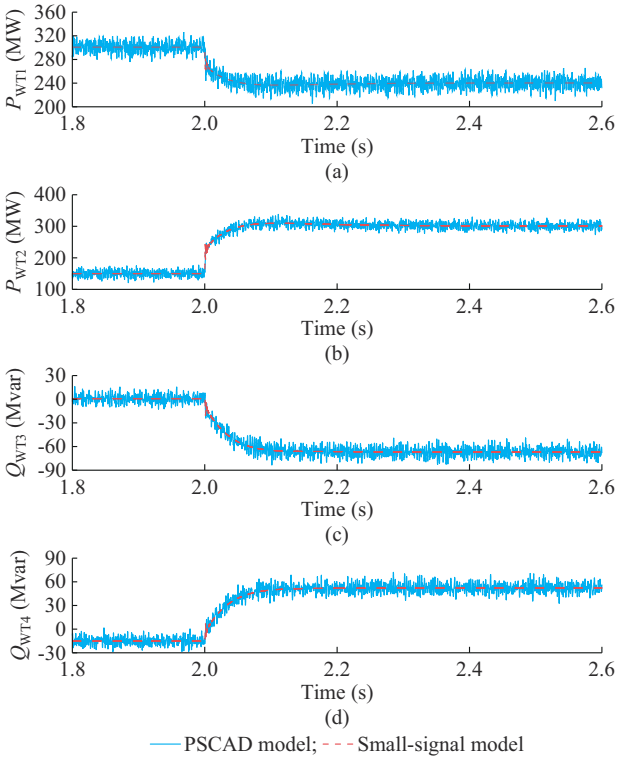

Fig. B1. Comparisons between small-signal model and PSCAD model. (a) Active power of WT1. (b) Active power of WT2. (c) Reactive power of WT3. (d) Reactive power of WT4.

REFERENCES

[1] GWEC. (2022, Jan.). Global offshore wind report 2022. [Online]. Available: https://gwec.net/gwecs-global-offshore-wind-report

[2] B. Yang, B. Liu, H. Zhou *et al*., "A critical survey of technologies of large offshore wind farm integration: summary, advances, and perspectives," *Protection and Control of Modern Power Systems*, vol. 7, no. 2, pp. 1-3, Apr. 2022.

[3] H. Lin, T. Xue, J. Lyu *et al*., "Impact of different AC voltage control modes of wind-farm-side MMC on stability of MMC-HVDC with offshore wind farms," *Journal of Modern Power Systems and Clean Energy*, vol. 11, no. 5, pp. 1687-1699, Sept. 2023.

[4] E. Apostolaki-Iosifidou, R. McCormack, W. Kempton *et al*., "Transmission design and analysis for large-scale offshore wind energy development," *IEEE Power and Energy Technology Systems Journal*, vol. 6, no. 1, pp. 22-31, Mar. 2019.

[5] R. Blasco-Gimenez, S. Anó-Villalba, J. Rodriguez-D'Derlée *et al*., "Diode-based HVDC link for the connection of large offshore wind farms," *IEEE Transactions on Energy Conversion*, vol. 26, no. 2, pp. 615-626, Jun. 2011.

[6] S. Bernal-Perez, S. Ano-Villalba, R. Blasco-Gimenez *et al*., "Efficiency and fault ride-through performance of a diode-rectifier- and VSC-inverter-based HVDC link for offshore wind farms," *IEEE Transactions on Industrial Electronics*, vol. 60, no. 6, pp. 2401-2409, Jun. 2013.

[7] O. Kuhn, P. Menke, R. Zurowski *et al*., "2nd generation DC grid access for offshore wind farms: HVDC in an AC fashion," *CIGRE Session*, vol. 2016, pp. 1-7, Jun. 2006.

[8] A. G. Siemens. (2015, Jan.). Siemens revolutionizes grid connection for offshore wind power plants. [Online]. Available: https:// www. 3blmedia. com/news/siemens-revolutionizes-grid-connection-offshore-wind-power-plants.

[9] T. H. Nguyen, D. C. Lee, and C. K. Kim, "A series-connected topology of a diode rectifier and a voltage-source converter for an HVDC transmission system," *IEEE Transactions on Power Electronics*, vol. 29, no. 4, pp. 1579-1584, Apr. 2014.

[10] M. von Hofen, D. Karwatzki, L. Baruschka *et al*., "Hybrid offshore HVDC converter with diode rectifier and modular multilevel converter," in *Proceedings of 2016 IEEE 7th International Symposium on Power Electronics for Distributed Generation Systems*, Vancouver, Canada, Jun. 2016, pp. 1-7.

[11] A. Nami, J. L. Rodriguez-Amenedo, S. Arnaltes *et al*., "Frequency control of offshore wind farm with diode-rectifier-based HVDC connection," *IEEE Transactions on Energy Conversion*, vol. 35, no. 1, pp. 130-138, Mar. 2020.

[12] T. H. Nguyen and N. T. Quach, "A hybrid HVDC converter based on M2C and diode rectifiers without DC capacitors for offshore wind farm integration," *International Journal of Electrical Power and Energy Systems*, vol. 133, p. 107260, Dec. 2021.

[13] A. Nami, J. L. Rodríguez-Amenedo, S. Arnaltes *et al*., "Hybrid HVDC system for offshore wind farms connection using series-connected diode rectifier units," in *Proceedings of 2019 21st European Conference on Power Electronics and Applications*, Genova, Italy, Sept. 2019, pp. 1-10.

[14] Y. Chang and X. Cai, "Hybrid topology of a diode-rectifier-based HVDC system for offshore wind farms," *IEEE Journal of Emerging and Selected Topics in Power Electronics*, vol. 7, no. 3, pp. 2116-2128, Sept. 2019.

[15] Z. Fang, X. Cai, X. Shi *et al*., "Diode rectifier-based hybrid high-voltage direct current converter for offshore wind farms," *IET Renewable Power Generation*, vol. 16, pp. 1-13, Nov. 2022.

[16] Y. Jin, Z. Zhang, Y. Huang *et al*., "Harmonic filtering and fault ride-through of diode rectifier unit and modular multilevel converter based offshore wind power integration," *IET Renewable Power Generation*, vol. 17, no. 14, pp. 3554-3567, Oct. 2023.

[17] M. Hoffmann, C. Rathke, A. Menze *et al*., "Parallel operation of HVDC DRU and VSC converters for offshore wind farm connection: technical and economic feasibility," in *Proceedings of 15th IET International Conference on AC and DC Power Transmission*, Coventry, UK, Feb. 2019, pp. 1-6.

[18] R. Li, L. Yu, L. Xu *et al*., "Coordinated control of parallel DR-HVDC and MMC-HVDC systems for offshore wind energy transmission," *IEEE Journal of Emerging and Selected Topics in Power Electronics*, vol. 8, no. 3, pp. 2572-2582, Sept. 2020.

[19] A. Nami, J. L. Rodriguez-Amenedo, S. Arnaltes *et al*., "Control of the parallel operation of DR-HVDC and VSC-HVDC for offshore wind power transmission," *IEEE Transactions on Power Delivery*, vol. 37, no. 3, pp. 1682-1691, Jun. 2022.

[20] L. Yu, R. Li, and L. Xu, "Hierarchical control of offshore wind farm connected by parallel diode-rectifier-based HVDC and HVAC links," *IET Renewable Power Generation*, vol. 13, no. 9, pp. 1493-1502, Jul. 2019.

[21] A. Bidadfar, O. Saborío-Romano, J. N. Sakamuri *et al*., "Coordinated control of HVDC and HVAC power transmission systems integrating a large offshore wind farm," *Energies*, vol. 12, no. 18, p. 3435, Sept. 2019.

[22] X. Cai, R. Yang, J. Zhou *et al*., "Review on offshore wind power integration via DC transmission," *Automation of Electric Power Systems*, vol. 45, no. 21, pp. 2-22, Nov. 2021.

[23] H. Zhang, W. Xiang, W. Lin *et al*., "Grid forming converters in renewable energy sources dominated power grid: control strategy, stability, application, and challenges," *Journal of Modern Power Systems and Clean Energy*, vol. 9, no. 6, pp. 1239-1256, Nov. 2021.

[24] H. Xiao, H. He, L. Zhang *et al*., "Adaptive grid-synchronization based grid-forming control for voltage source converters," *IEEE Transactions on Power Systems*, vol. 39, no. 2, pp. 4763-4766, Mar. 2024.

[25] L. Yu, R. Li, and L. Xu, "Distributed PLL-based control of offshore wind turbines connected with diode-rectifier-based HVDC systems," *IEEE Transactions on Power Delivery*, vol. 33, no. 3, pp. 1328-1336, Jun. 2018.

[26] R. Li, L. Yu, and L. Xu, "Offshore AC fault protection of diode rectifier unit-based HVDC system for wind energy transmission," *IEEE Transactions on Industrial Electronics*, vol. 66, no. 7, pp. 5289-5299, Jul. 2019.

[27] L. Yu, R. Li, L. Xu *et al*., "Analysis and control of offshore wind farms connected with diode rectifier-based HVDC system," *IEEE Transactions on Power Delivery*, vol. 35, no. 4, pp. 2049-2059, Aug. 2020.

[28] A. Bidadfar, O. Saborío-Romano, N. A. Cutululis *et al*., "Control of offshore wind turbines connected to diode-rectifier-based HVDC systems," *IEEE Transactions on Sustainable Energy*, vol. 12, no. 1, pp. 514-523, Jan. 2021.

[29] L. Yu, L. Xu, J. Zhu *et al*., "Impedance modelling and stability analysis of diode-rectifier based HVDC connected offshore wind farms," *IEEE Transactions on Power Delivery*, vol. 37, no. 1, pp. 591-602, Feb. 2022.

[30] Z. Zhang, Y. Tang, and Z. Xu, "Medium frequency diode rectifier unit based HVDC transmission for offshore wind farm integration," *IET Renewable Power Generation*, vol. 15, no. 4, pp. 717-730, Mar. 2021.

[31] Y. Tang, Z. Zhang, and Z. Xu, "DRU based low frequency AC transmission scheme for offshore wind farm integration," *IEEE Transactions on Sustainable Energy*, vol. 12, no. 3, pp. 1512-1524, Jul. 2021.

[32] M. Yang, X. Cai, A. Wusiman *et al*., "Distributed-diode-rectifiers-based offshore wind power MVDC direct-transmission system," *IEEE Transactions on Energy Conversion*, vol. 37, no. 1, pp. 643-653, Mar. 2022.

[33] M. Á. Cardiel-Álvarez, S. Arnaltes, J. L. Rodriguez-Amenedo *et al*., "Decentralized control of offshore wind farms connected to diode-based HVDC links," *IEEE Transactions on Energy Conversion*, vol. 33, no. 3, pp. 1233-1241, Sept. 2018.

[34] A. P. Asensio, S. A. Gómez, J. L. Rodriguez-Amenedo *et al*., "Reactive power synchronization method for voltage-sourced converters," *IEEE Transactions on Sustainable Energy*, vol. 10, no. 3, pp. 1430-1438, Jul. 2019.

[35] H. Xiao, X. Huang, Y. Huang *et al*., "Self-synchronizing control and frequency response of offshore wind farms connected to diode rectifier based HVDC system," *IEEE Transactions on Sustainable Energy*, vol. 13, no. 3, pp. 1681-1692, Jul. 2022.

[36] Z. Zhang, Y. Jin, and Z. Xu, "Grid-forming control of wind turbines for diode rectifier unit based offshore wind farm integration," *IEEE Transactions on Power Delivery*, vol. 38, no. 2, pp. 1341-1352, Apr. 2023.

[37] Y. Jin, Z. Zhang, H. Wu *et al*., "Black start strategy of offshore wind farm based on grid-forming wind turbines and diode rectifier unit," *High Voltage Engineering*, vol. 49, no. 9, pp. 3730-3740, Sept. 2023.

[38] Z. Xu, "Main schemes and key technical problems for grid integration of offshore wind farm," *Automation of Electric Power Systems*, vol. 46, no. 21, pp. 1-10, Nov. 2022.

[39] J. Martínez-Turégano, S. Añó-Villalba, S. Bernal-Perez *et al*., "Small-signal stability and fault performance of mixed grid forming and grid following offshore wind power plants connected to a HVDC-diode rectifier," *IET Renewable Power Generation*, vol. 14, no. 12, pp. 2166-2175, Sept. 2020.

[40] B. Wu, Y. Lang, N. Zargari *et al*., *Power Conversion and Control of Wind Energy Systems*. New York: John Wiley and Sons, 2011.

[41] Z. Zhang, Q. Chen, Y. Jin *et al*., "Optimal operation frequency for medium frequency grid-following offshore wind farm integrated by MMC-HVDC," *Power System Technology*, vol. 46, no. 8, pp. 2881-2888, Aug. 2022.

Yanqiu Jin received the B. S. degree in electrical engineering from Shandong University, Jinan, China, in 2020. She is currently working towards the Ph.D. degree in electrical engineering from Zhejiang University, Hangzhou, China. Her research interests include high-voltage direct current (HVDC) and grid integration of renewable energy.

Zheren Zhang received the B.S. and Ph.D. degrees in electrical engineering from Zhejiang University, Hangzhou, China, in 2011 and 2016, respectively. He is now with the Department of Electrical Engineering, Zhejiang University. His research interests include HVDC, flexible AC transmission system, and grid integration of renewable energy.

Zheng Xu received the B. S., M. S., and Ph. D. degrees in electrical engineering from Zhejiang University, Zhejiang, China, in 1983, 1986, and 1993, respectively. He has been with the Department of Electrical Engineering, Zhejiang University, since 1986 and has been a Professor there since 1998. He is a Fellow of IEEE for his contributions to control and modeling of multilevel converter (MMC) based HVDC transmission systems. His research interests include HVDC transmission, power system dynamics, and grid integration of renewable energy.